

Electronic supplementary information

Photon-induced generation and spatial control of extreme pressure at the nanoscale with a gold bowtie nano-antenna platform

Christos Boutopoulos^{1,2}, Adrien Dagallier¹, Maria Sansone^{1,3}, Andre-Pierre Blanchard-Dionne¹,
Évelyne Lecavalier-Hurtubise¹, Étienne Boulais^{1,4}, Michel Meunier^{1*}

¹*Laser Processing and Plasmonics Laboratory, Department of Engineering Physics, Polytechnique
Montréal, Montréal, Québec H3C 3A7, Canada*

²*SUPA, School of Physics and Astronomy, University of St. Andrews, North Haugh, St. Andrews,
KY16 9SS, UK*

³*Dipartimento di Chimica "A.M. Tamburro", Università della Basilicata, Viadell'Ateneo Lucano
10, 85100 Potenza, Italy*

⁴*Laboratory of Biosensors and Nanomachines, Department of Chemistry, Université de
Montréal, Montréal, Québec, H3T 1J4, Canada*

1. The effect of the flare angle variation on the AuBT optical response

The selection of 60 degree flare angle (black dot in Figure S1) is in accordance with our optimization criteria for a given wavelength ($\lambda=800\text{nm}$), i.e., (i) to minimize the absorption cross-section in order to avoid thermal damage and (ii) to maximize the near-field enhancement in order to enhance non-linear interaction with water molecules and pressure generation. Note that the AuBT optical response only slightly depends on the flare angle for transversal polarization (Figure S1b and S1d), while for longitudinal polarization the selection of 60° ensured the need of relatively high near-field and low absorption cross-section for a given wavelength ($\lambda = 800 \text{ nm}$) (Figure S1a and S1c).

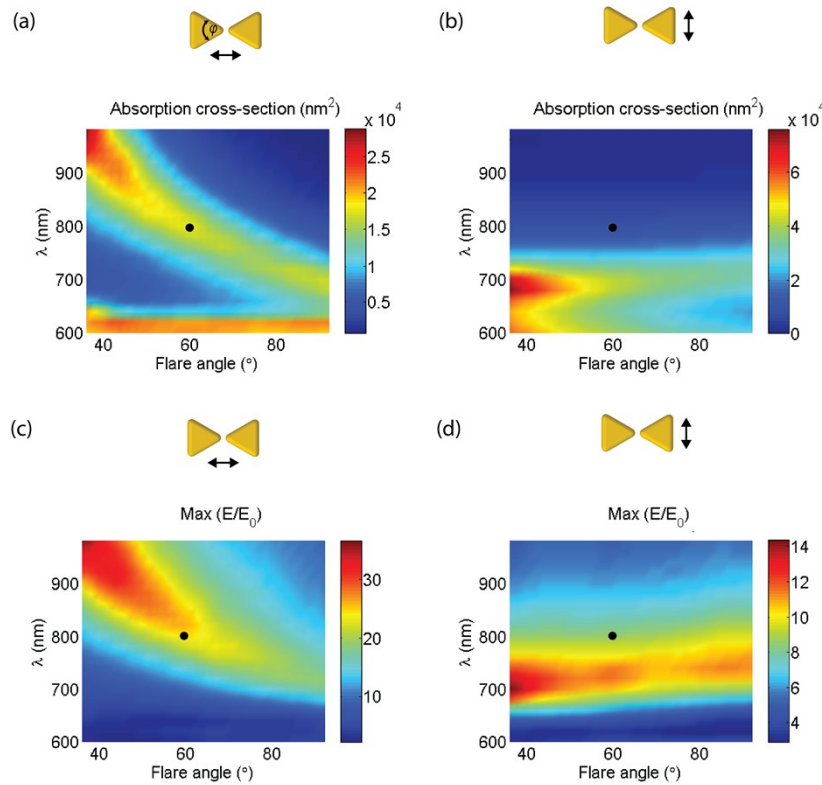


FIGURE S1: The effect of the flare angle variation on the optical response of the AuBT. (a) Absorption cross-section and maximum near-field amplification for longitudinal ((a) and (c)) and transversal polarization ((b) and (d)). The black dot indicates the selected AuBT design, which represents a compromise of relatively high near-field and low absorption cross-section for a given wavelength ($\lambda = 800 \text{ nm}$).

2. Spectroscopic characterization of individual AuBTs

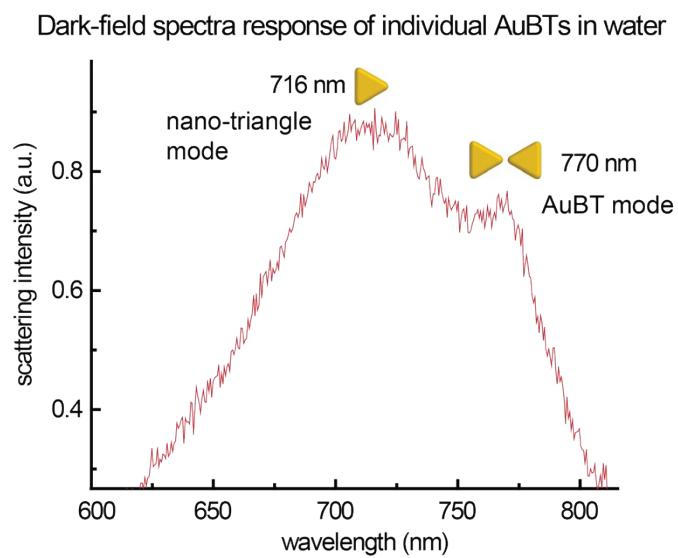


FIGURE S2: Spectra response (scattering) of individual AuBTs ($L = 100 \pm 3$ nm, $G = 20 \pm 2$ nm, average of six individual AuBT spectra) under non polarization-resolved dark-field excitation.

3. Experimental setup for time-resolved shadowgraphic imaging of nanobubbles

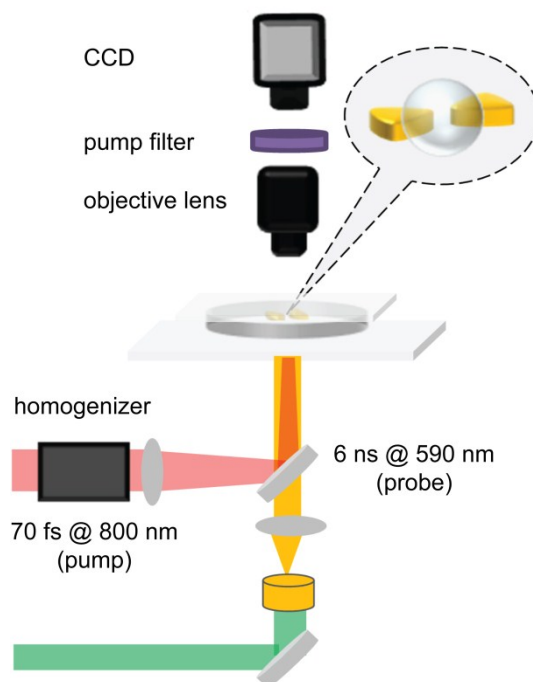


FIGURE S3: Schematic representation of the experimental setup used for the AuBT irradiation and nanobubble detection.

4. Plasmon shielding effect on the AuBT absorption cross-section and plasma cross-section

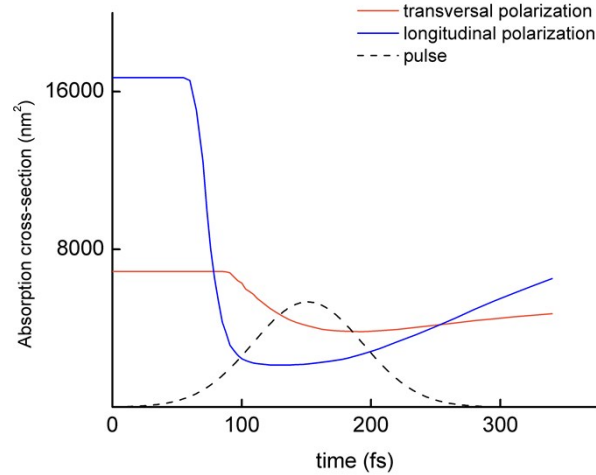


FIGURE S4: The plasmon shielding effect on the AuBT absorption cross-section for laser irradiation at 120 mJ/cm^2 with longitudinal and transversal polarizations. The dashed line indicates the fs laser pulse (in a.u.)

5. AuBT displacement simulation

We consider the following mechanism to explain the SEM observations. Nano-triangles are being melted after the AuBTs excitation and rapidly converted into nanospheres. The melted spheres can now move directionally according to the resultant force, generated by the polarization dependent optical breakdown. Finally, nanosphere solidification occurs (within few ns), which ensures good adhesion to the substrate. Simplified modelling of the proposed mechanism was performed by considering the motion of the spherical gold nanostructures in water, under the resulting force for diagonal polarization (DP) excitation. The simulation calculates the temperature in the water at every point of the computational mesh (see section 7). Assuming the duration of the simulation is short enough to consider water undergoes an isochoric phase transformation, the thermodynamic variables are functions of the temperature only. We used the SESAME¹ equation of states to get the pressure and heat capacity at constant volume. We calculated the force acting to the AuBT centre of mass by integrating the pressure over the whole surface of the nanostructure (Figure S5a).

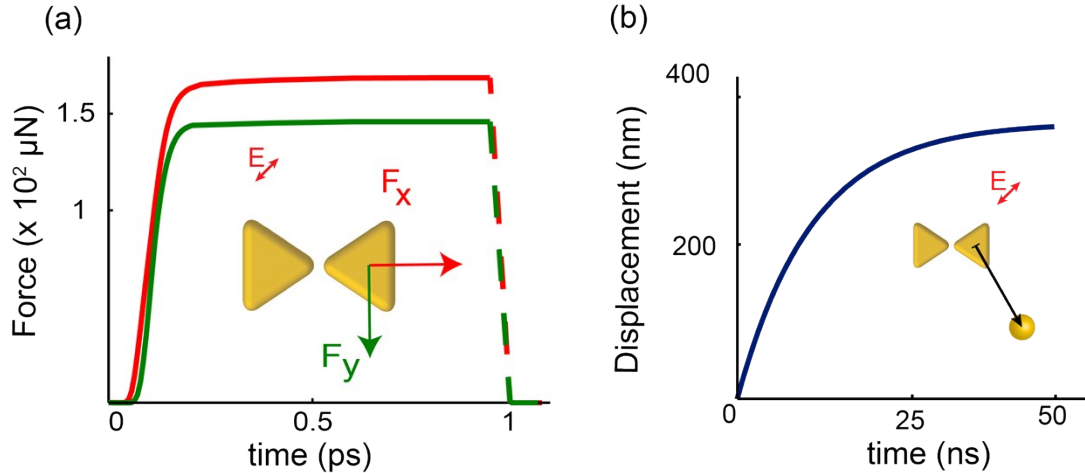


FIGURE S5: Laser excitation of AuBT at 120mJ/cm² with diagonal polarization. (a) Simulated resultant force applied to the centre of mass and (b) displacement of the nano-triangle.

Plasma dynamics relax within the first 1 ps, and since plasma plays the dominant role in pressure generation² we considered the force to be applied during 1 ps only. Once in motion, the gold nanostructure is slowed down by the viscous friction of the surrounding water. This is modeled with the $6\pi\mu Rv$ Stokes' law, with v the velocity of the individual AuBT. The radius R is calculated assuming the nano-triangle is transformed into nano-sphere (it can be safely assumed from the SEM images, Figure 4) of same volume, and μ is the dynamic viscosity of water at resting temperature. We therefore solve the equation $m\dot{v} = F - 6\pi\mu Rv$, and integrate again to get the position of the nano-sphere centre as a function of the time (Figure S5b). The displacement was calculated up to 50 ns, which represents the time frame in which the gold nano-spheres reach their final position. The simulated displacement value (~ 350 nm) is in agreement with the corresponding values obtained with SEM (~ 120 nm). The simulation yield larger value, which was to be expected since the friction at the ITO interface was not taken into account.

6. AuBT damage and correlation with nanobubble detection

SEM pictures were taken from single pulse treated AuBT samples (bubble threshold fluence 70 mJ/cm², longitudinal polarization) and correlated with the corresponding pump-probe images (Figure S6). Since we applied threshold laser fluence, the slight variation in the morphology of neighbouring AuBTs resulted in significant variation to the bubble generation efficacy. This is shown in Figure S6 where only two out of four marked neighbouring AuBT generated bubbles. The corresponding SEM pictures revealed that AuBT remained intact when no bubble was generated (insets III. and IV. in Figure S6), while bubble generation resulted in alteration of their morphology (insets II. and II in Figure S6). In

accordance with those results, routine SEM observations (data not shown) did not show any noticeable alteration of the AuBT morphology when the excitation laser fluence was kept below the cavitation threshold (70 mJ/cm²)

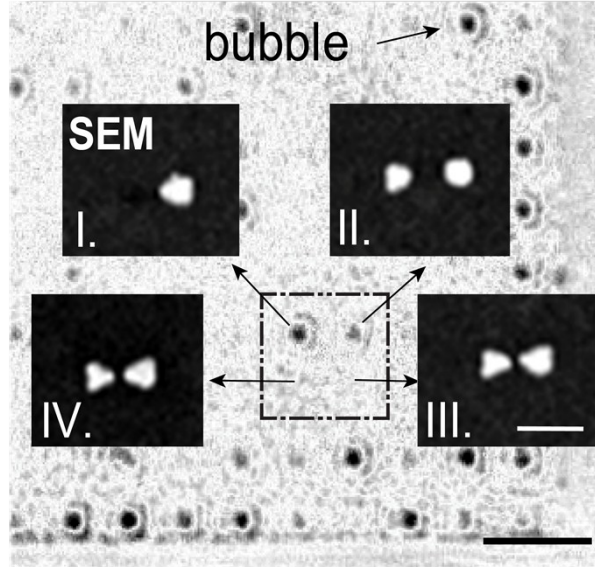


FIGURE S6: Superposition of a nanobubble detection image and SEM pictures of individual AuBTs. Nanobubbles were detected 15 ns after the excitation of AuBT sample with a single 70 fs pulse at 70 mJ/cm². SEM pictures were captured after the laser irradiation. The inset SEM pictures (I) and (II) correspond to bubble generating AuBTs, while insets (IV) and (III) correspond to non-bubble generating AuBTs. The scale bar in the shadowgraphic image corresponds to 20 μm, while the one for all SEM pictures corresponds to 200 nm.

7. AuBT modeling: plasma dynamics, TTM, ITO layer and computational domain

The model used for this article is similar to the one published by Boulais et al.³. The electromagnetic

field E is computed in 3D on the whole computational domain using the vector Helmholtz equation,

$$\nabla \times (\nabla \times E) - k_0^2 \epsilon_r E = 0$$

Gold optical properties are taken from ref⁴ and assumed constant. The complex relative permittivity of the water, ϵ_r , is time-dependent and includes the effect of the free electrons generated in the water close to the nanostructure³:

$$\epsilon_r = \left[n_w^2 - \frac{\omega_p^2}{\omega^2 + \nu_e^2} \right] - i \left[\frac{\omega_p^2 \omega \nu_e}{\omega^4 + \omega^2 \nu_e^2} \right], \text{ where } n_w \text{ is water's refractive index at rest, } \omega_p \text{ is the plasmon}$$

frequency $\sqrt{\frac{n_e e^2}{m_e \epsilon_0}}$ and ν_e is the total collision frequency, sum of the collision frequencies with ions (ν_{ei} , defined in ref⁵) and neutral water molecules (ν_{en} , defined in ref^{6,7}). The electromagnetic field is calculated at each time step using this time-dependent water permittivity.

The AuBT's response to the irradiation is calculated using a parabolic Two-Temperature Model (TTM)⁸, with the two temperatures T_e and T_{Au} respectively designating the temperatures of the quasi-free electrons and of the gold lattice ions:

$$\begin{cases} C_e \rho_e \frac{\partial T_e}{\partial t} - \nabla \cdot (k_e \nabla T_e) = Q_{EM} - \Gamma(T_e - T_{Au}) \\ C_{Au} \rho_{Au} \frac{\partial T_{Au}}{\partial t} - \nabla \cdot (k_{Au} \nabla T_{Au}) = \Gamma(T_e - T_{Au}) \end{cases}$$

Q_{EM} refers to resistive losses in the nanostructure. A conductive heat flux at the gold-water interface is implemented. The electrons collective oscillations in the nanostructure redistribute the incident field in the near-field⁹. Locally, the electromagnetic field can be greatly enhanced (23 times in Figure 3(c) of the main text, for instance). These extreme fields lead to ionization of a nanoplasma^{3,10}. Following ref^{11,12}, we consider that water behaves as a semiconductor with a 6.5 eV gap. We use the Keldysh theory and a dense plasma formalism⁶ to account for the spatial and temporal evolution of the electronic density n_e ,

$$\frac{\partial n_e}{\partial t} + \nabla \cdot (D_e \nabla n_e) = S_{photo} + S_{coll} - S_{rec}$$

and the electronic energy density u ,

$$\frac{\partial u}{\partial t} + \nabla \cdot (D_u \nabla u) = Q_{EM} - Q_{ei} - Q_{rad} - \tilde{\Delta} S_{coll}$$

where S_{photo} is the Keldysh photoionization term, including multiphoton and tunnel ionization¹³, S_{coll} is the avalanche ionization term⁶, S_{rec} is the recombination term¹¹, Q_{EM} is the energy absorption through inverse Bremsstrahlung¹¹, Q_{ei} is the term accounting for the energy losses through collisions with ions^{7,14} and Q_{rad} is the radiative losses⁷. The aforementioned conductive heat transfer at the interface, electron-ions collisions and recombination losses act as source term to calculate the temperature in the water through a heat equation. Heat conduction and

convection is neglected, due to the very short duration of the simulation:

$$\rho_w C_w \frac{\partial T_w}{\partial t} = Q_{ei} + S_{rec} \left(\tilde{\Delta} + \frac{u}{n_e} \right) \tilde{\Delta}$$

is the effective ionization potential in water, from Keldysh theory.

The computational domain used in our simulation model is shown in Figure S7. The role of the transparent 100 nm ITO layer was thoroughly investigated in our modelling. The ITO layer refractive index was taken from ref¹⁵. In an alternative model, we approximated the ITO layer as a 3.6 to 4.2 eV gap semiconductor¹⁶⁻¹⁹, and the plasma dynamics within ITO was simulated using a formalism similar to ref²⁰. However, the good agreement between the simulations without considering the excitation of high energy electrons in the ITO layer and the experimental results of polarization-independent cavitation threshold, plus the fact that SEM images clearly show that the ITO layer is not damaged after the irradiation, led us to completely neglect the direct ionization of the ITO layer in our model.

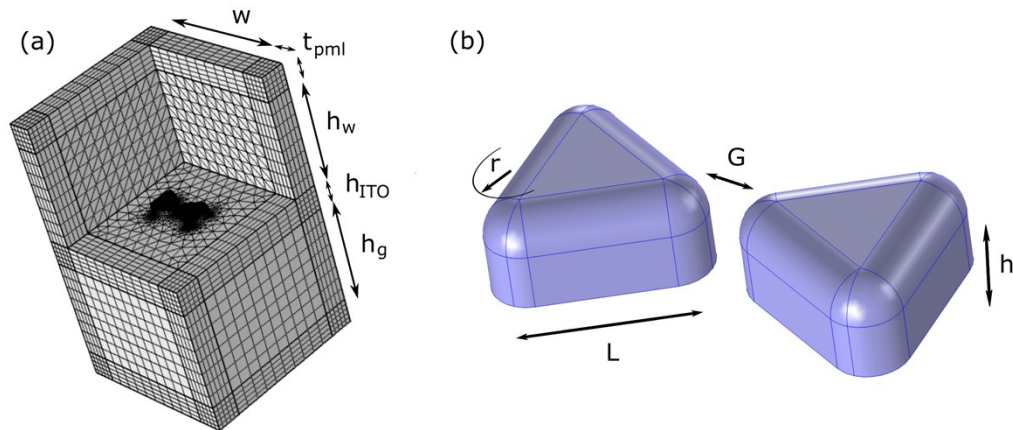


FIGURE S7: (a) Computational domain ($W=500$ nm, $t_{pml}=100$ nm, $h_w=400$ nm, $h_{ITO}=100$ nm, $h_g=400$ nm) and (b) AuBT geometry used in the modelling ($r=20$ nm, $G=20$ nm, $L=100$ nm, $h=50$ nm).

References

- 1 SESAME: The Los Alamos National Laboratory Equation-of-State Database, Report No. ucrl-7118 and ucrl-52190; Lyon, S. P., Johnson, J. D., Eds.; Los Alamos National Laboratory: Los Alamos, NM, 1979. The water table used here was SESAME table 7150.
- 2 V. Zhigilei and B. J. Garrison, *MRS Proc.*, 1998, **538**, 491.
- 3 E. Boulais, R. Lachaine and M. Meunier, *Nano Lett.*, 2012, **12**, 4763–9.
- 4 P. B. Johnson and R. W. Christy, *Phys. Rev. B*, 1972, **6**, 4370–4379.
- 5 Y. T. Lee and R. M. More, *Phys. Fluids*, 1984, **27**, 1273.
- 6 L. Hallo, A. Bourgeade, V. T. Tikhonchuk, C. Mezel and J. Breil, *Phys. Rev. B - Condens. Matter Mater. Phys.*, 2007, **76**, 1–12.
- 7 N. E. Andreev, M. E. Veisman, V. P. Efremov and V. E. Fortov, *High Temp.*, 2003, **41**, 594–608.
- 8 N. Singh, *Int. J. Mod. Phys. B*, 2010, **24**, 1141–1158.
- 9 M. I. Stockman, *Opt. Express*, 2011, **19**, 22029.
- 10 K. Ostrikov, F. Beg and A. Ng, *Rev. Mod. Phys.*, 2016, **88**, 1–22.
- 11 A. Vogel, J. Noack, G. Hüttman and G. Paltauf, *Appl. Phys. B*, 2005, **81**, 1015–1047.
- 12 C. A. Sacchi, *J. Opt. Soc. Am. B*, 1991, **8**, 337.
- 13 L. Keldysh, *JETP*, 1965, **20**, 1018–1026.
- 14 M. Veysman, B. Cros, N. E. Andreev and G. Maynard, *Phys. Plasmas*, 2006, **13**.
- 15 T. A. F. König, P. A. Ledin, J. Kerszulis, M. A. Mahmoud, M. A. El-Sayed, J. R. Reynolds and V. V. Tsukruk, *ACS Nano*, 2014, **8**, 6182–6192.
- 16 S. H. Brewer and S. Franzen, *Chem. Phys.*, 2004, **300**, 285–293.
- 17 K. Ellmer and R. Mientus, *Thin Solid Films*, 2008, **516**, 4620–4627.
- 18 M. S. Farhan, E. Zalnezhad, A. R. Bushroa and A. A. D. Sarhan, *Int. J. Precis. Eng. Manuf.*, 2013, **14**, 1465–1469.
- 19 F. R. Chowdhury, S. Choudhury, F. Hasan and T. Begum, *J. Bangladesh Acad. Sci.*, 2011, **35**, 99–111.
- 20 N. M. Bulgakova, R. Stoian, A. Rosenfeld, I. V. Hertel and E. E. B. Campbell, *Phys. Rev. B*, 2004, **69**, 054102.